An X-Band Leaky-Wave Dynamic Metasurface Antenna for Integrated Sensing and Communication

Praneet Jain*, Trung Q. Duong†*, Saptarshi Ghosh‡, Peng-Yuan Wang§, Simon Cotton*, Okan Yurduseven*
*Center for Wireless Innovation, Queen's University Belfast, Belfast, UK, pjain02@qub.ac.uk
†Faculty of Engineering and Applied Science, Memorial University of Newfoundland, St. John's, Canada
‡Dept. of Electrical Engineering, Indian Institute of Technology Indore, Indore, India
§Department of Electrical and Electronic Engineering, University of Nottingham Ningbo China, China

***Abstract*—The work demonstrates a dynamic metasurface antenna (DMA) that consists of hexagonal-shaped meta-atoms. The hexagonal-shaped meta-atoms are arranged in a diagonal fashion in the top layer of the substrate integrated waveguide (SIW). The SIW feeds an array of 32 such meta-atoms. By using p-i-n diodes, the radiation characteristic and the interaction with the propagating wave of each meta-atom are varied in two states. The DMA is capable of generating 7 distinct beam patterns by biasing the p-i-n diodes with the binary distributions obtained through holographic approximation. The DMA offers a wide beam coverage of 136° and an average gain of 6.3 dBi for all the binary distributions. Furthermore, the DMA demonstrates direction-of-arrival (DoA) detection for one or two simultaneous sources with an error as low as 1°. Full-wave simulations validate the design, highlighting its potential for integrated sensing and communication (ISAC) applications.**

***Index Terms*—beamcoverage, ISAC, metasurfaces, meta-atoms, reconfigurable, p-i-n diodes.**

I. INTRODUCTION

Integrated Sensing and Communication (ISAC) is expected to play a key role in enabling new functionalities for 6G services [1], [2]. Sensing in wireless systems can take various forms, including human activity recognition [3], vital sign monitoring [4], direction of arrival (DoA) estimation of transmitting sources [5], [6], localization and tracking [7], [8]. A wireless system that can sense its environment and adapt accordingly not only enhances communication reliability but also improves system throughput. Achieving this requires radio frequency (RF) hardware capable of supporting both communication and sensing tasks.

Several antenna designs have been proposed for ISAC. For example, full-duplex or simultaneous transmit-and-receive (STAR) antennas provide isolated channels for transmitting and receiving electromagnetic (EM) signals, typically through two physically separated antenna elements [9], [10], [11]. Another promising category is Dynamic Metasurface Antennas (DMAs), which employ a spatial distribution of meta-atoms to achieve reconfigurable radiation characteristics. In [12] a reconfigurable DMA is introduced which utilizes compressive sensing techniques for DoA sensing and imaging. Subsequently, in [13], a substrate integrated waveguide (SIW)-fed DMA is presented, resonating at 5.1 GHz and offers a wide beam coverage. Other works [14], [15], [16] have explored SIW-based DMAs across different bandwidths and meta-atom designs. These SIW-based DMAs enable azimuthal-plane scanning of transmitting sources and directional beamforming for communication, making them strong candidates for ISAC applications.

The DMA presented in this work employs a hexagonal-shaped meta-atom to achieve beam steering in X-band, with a wide beam coverage of 136°. It is further characterized for DoA sensing, achieving an estimation error of up to 1° for a single source in the azimuthal plane, as well as for two simultaneously transmitting sources with the same precision. This combination of wide beam coverage and high DoA accuracy highlights the suitability of the proposed antenna for ISAC applications.

II. RECONFIGURABLE ANTENNA DESIGN

A. DMA Design

The Fig.1 demonstrates the proposed SIW-based DMA antenna design, which consists of 32 complementary electric inductive capacitive (cELC) meta-atoms arranged periodically on the top layer of the SIW. The p-i-n diodes from MACOM semiconductors, MA4SPS402 [17], are mounted across the meta-atoms for controlling their radiation response. The SIW cavity is fed using a microstrip line with a tapered transition. As compared to a microstrip waveguide, which supports quasi TE_{10}, the SIW supports a true TE_{10} mode, which makes them optimum for exciting the cELC meta-atoms [18]. The hexagonal-shaped meta-atoms are placed symmetrically along the central line of the structure (x-axis) to minimize wave perturbation of the propagating wave and reduce inter-cell interaction. The number of elements is also selected in order to have a sufficiently large electrical aperture with a reasonable antenna size. Rogers R4003C (ε_r = 3.55 and $\tan\delta$ = 0.0027) is chosen as the constituent dielectric with copper cladding on both sides for the antenna design.

B. Meta-Atom Design and Simulation Response

The constituent meta-atoms of the DMA are obtained by taking the complement of the electric–inductive–capacitive (ELC) resonator, as illustrated in Fig. 2(a). The ELC structure consists of a hexagonal ring with T-shaped inserts positioned such that their wider portions face each other across a narrow gap. These wider portions act as capacitors when excited by an electric field oriented along the y-axis, while the hexagonal

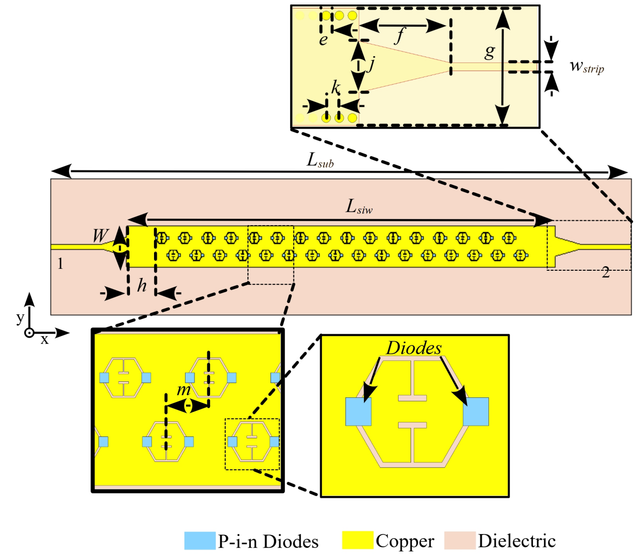

Fig. 1. Schematic of the DMA antenna design. The illustrated dimensions are as follows:-e = 1.4 mm, f = 10.8 mm, g = 18 mm, h = 12.7 mm, j = 8.4 mm, k = 2.1 mm, m = 5.1 mm, W = 60 mm, w_{strip} = 2.2 mm, L_{siw} = 189 mm and L_{sub} = 256 mm.

ring provides inductive response to a magnetic field along the x-axis. Consequently, the structure behaves as a parallel LC resonator for an incident electromagnetic (EM) wave propagating in the –ve z-direction. According to Babinet's principle, its complementary structure exhibits the dual response, operating as a series LC resonator that couples strongly to the magnetic field component [19].

Fig. 2(b) shows the scattering parameter (S-parameter) response of the complementary meta-atom under periodic boundary conditions, with magnetic boundaries along the z-axis, electric boundaries along the y-axis, and ports defined along the x-axis. The resonance occurs at 9.8 GHz, where the structure behaves analogously to a series LC circuit. In other words it behaves as a short circuit at resonance, enabling wave transmission, while attenuating off-resonant frequencies. The resonance frequency can be tuned by adjusting the hexagonal ring dimensions or the gap between the T-shaped inserts.

Subsequently, a single element of the meta-atom is embedded in an SIW with p-i-n diodes to observe the control over the radiation characteristics. The operational spectrum of the antenna is influenced by the resonant frequency of the meta-atom and the off-state (C_{OFF}) capacitance of the p-i-n diode as well. Fig. 3(a) depicts the normalized radiated power when the biasing state of the p-i-n diodes is varied, and Fig. 3(b) represents the simulation setup. The p-i-n diodes are modelled as an RL circuit with R_{ON} = 7 Ω and L_{ON} = 0.45 nH, during the forward biased state, and, in the reverse biased state, as an LC circuit with L_{OFF} = 0.45 nH and C_{OFF} = 0.01 pF [17]. It can be observed that when the p-i-n diodes are reverse biased or in the OFF state, the element radiates (element is in the ON state) with maximum radiated power at 10.7 GHz. Subsequently, when the p-i-n diodes are forward biased, the element is in the OFF state and ceases radiation. It can be observed that the radiated power is almost 10 dB higher when the element is in the ON state as compared to when it is in the OFF state.

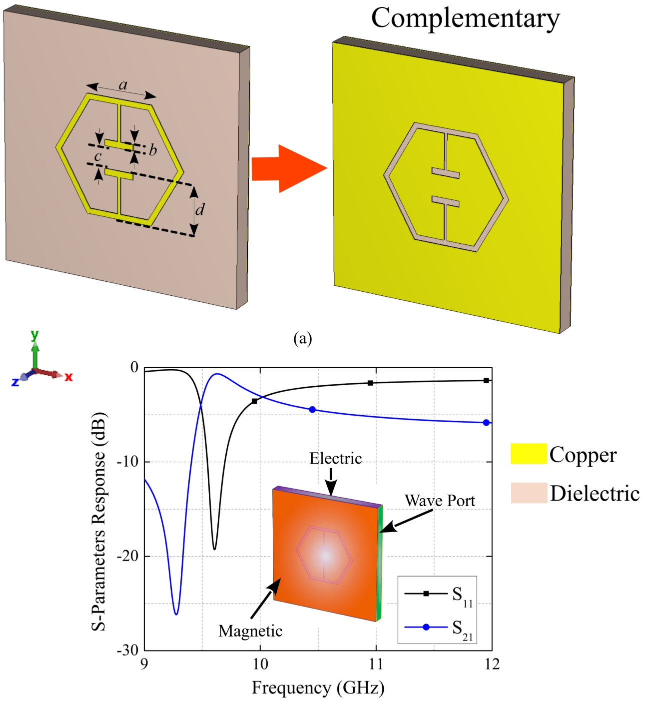

(a)

(b)

Fig. 2. (a) Hexagonal-shaped unit cell design and it's complementary structure. The illustrated dimensions are as follows:- a = 2.75 mm, b = 0.25 mm , c = 0.9 mm and d = 1.93 mm . (b) S-parameter response of the meta-atom. The boundary conditions are shown in the inset of the figure.

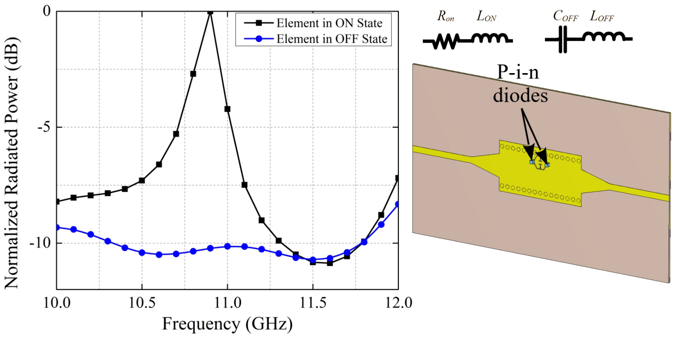

(a)

(b)

Fig. 3. (a) Normalized radiated power plot for different biasing states of the p-i-n diodes. (b) Schematic for simulation with pi-n diodes (R_{ON} =7 Ω , L_{ON} = 0.45 nH , C_{OFF} = 0.01 pF and L_{OFF} = 0.45 nH)

III. Simulation and Radiation Pattern Results

A. S-Parameter Response

Fig. 4 demonstrates the S-parameter response of the DMA for different biasing states of the p-i-n diodes. Fig. 4(a) illustrates the S-Parameters obtained when all the p-i-n diodes are reverse biased (elements are in ON state), and Fig. 4(b) shows the S-Parameters when all the p-i-n diodes are forward

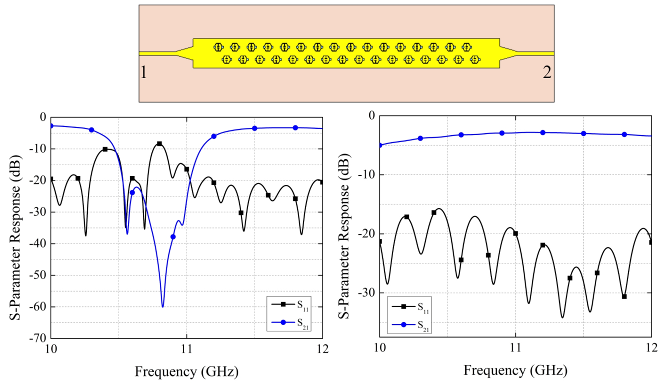

(a) (b)

Fig. 4. S-Parameter response of the developed DMA antenna, (a) when all the p-i-n diodes are reverse biased, and (b) when all the p-i-n diodes are forward biased.

TABLE I
HEXADECIMAL CODES FOR BEAM GENERATION

Case No.	Hexadecimal Code	Intended Beam Direction	Simulated Beam Direction
1	DB6DB6DB	5°	7°
2	D2DA5B4B	15°	18°
3	94B5AD69	20°	23°
4	B52A56AD	30°	31°
5	A556AA55	40°	41°
6	AA55556A	50°	49°
7	AAAAAAAA	60°	63°

biased (elements are in OFF state). It can be observed that when all the p-i-n diodes are forward biased, the entire antenna behaves as a typical waveguide; conversely, when all the p-i-n diodes are reverse biased, a dip in S_{21} can be observed at the intended frequency, indicating the coupling to the propagating wave in the waveguide. The S_{11} values are also below -10 dB in both the cases, demonstrating good match to the input ports.

B. Radiation Pattern Results

The cELC meta-atoms can be modeled as magnetic dipoles that couple strongly to the magnetic component of the propagating wave. A holographic approximation on the polarization of the meta-atoms can be used for beamforming in the intended direction [13], [20], [21]. Subsequently, by using a heaviside function, a binary distribution for forming beam in the desired direction can be obtained. A detailed description can be found in the ref. [20] and [21]. Table I lists the hexadecimal equivalents of the binary distributions derived for different beam directions. Here, "1" indicates a forward-biased diode (element is in OFF state), while "0" corresponds to a reverse-biased state (element is in ON state).

Fig. 5 plots the simulated radiation pattern for the different cases as mentioned in Table I. As can be seen in Fig. 5, the obtained radiation patterns from the DMA closely follow the intended scan angles throughout the studied biasing cases. Slight differences in the point angles can be attributed to inter-cell interactions and wave scattering from the meta-atoms, which are difficult to model while extracting the binary codes for the intended beam directions. The antenna has an average gain of 6.3 dBi and an average simulated radiation efficiency of 42% over all the studied cases. The overall beam coverage of the antenna is 136° when the antenna is fed from both ports.

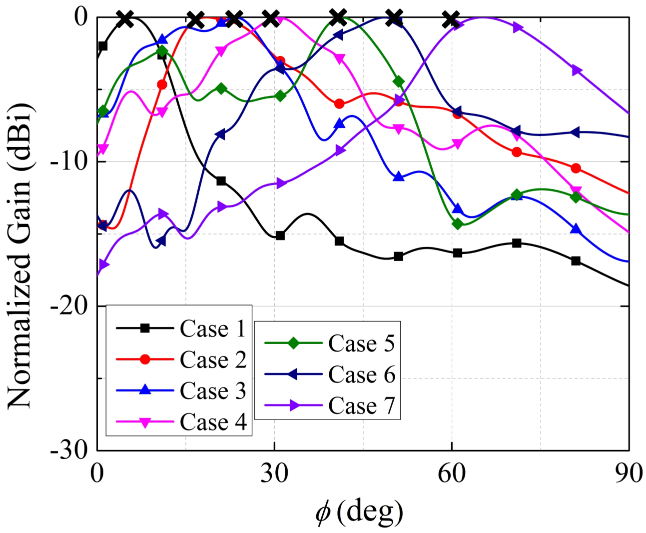

Fig. 5. Simulated radiation patterns of the DMA in E-plane (xz-plane) for the different biasing cases provided in Table I. The cross marks indicate the intended beam directions.

IV. DOA SENSING RESPONSE

The wide beam coverage of the DMA can be leveraged to estimate the direction of arrival (DoA) of nearby sources. Specifically, the 1-D DMA enables estimation of the azimuthal angle by solving eq. (1),

$$\mathbf{g} = \mathbf{H}\mathbf{f}. \tag{1}$$

In (1), the bold font is used to denote the vector-matrix notation. Here, $\mathbf{g}$ is a column vector of size $(m, 1)$ containing the amplitudes of the received signal at 10.7 GHz for m different radiation patterns ($m = 7$ in this case). $\mathbf{H}$ in (1) is an $m \times n$ matrix where each element in a row corresponds to the magnitude of the received signal at the n^{th} angle, while the m^{th} row corresponds to the m^{th} case (hexadecimal code) listed in Table I. The vector $\mathbf{f}$ is the unknown column vector of size $(n, 1)$ representing the angular spectrum across n angle bins [22], [23].

Due to the antenna's symmetry, only a quadrant of the azimuthal plane is considered, with the angular space discretized into 1° bins. Since $\mathbf{H}$ is not square, equation 1 is solved using the generalized minimum residual method (GMRES) [24]. Fig. 6 shows the estimated DoA for a single-source scenario under three cases: 10°, 32°, and 50°. The corresponding estimated angles are 9°, 32°, and 51°, respectively. All reported angles refer to the azimuthal plane of the antenna, as depicted in Fig. 6.

A multi-source scenario is also investigated, considering two simultaneous transmissions at 25° and 50°. The corresponding

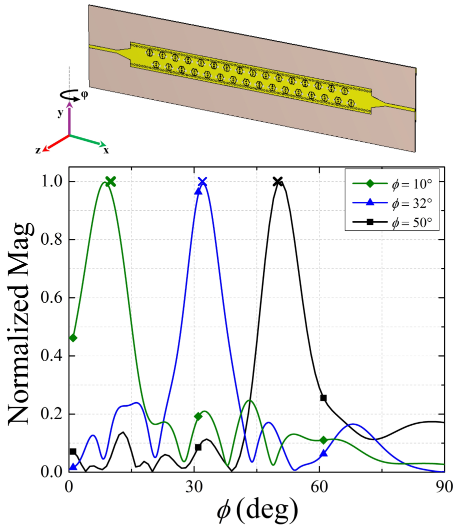

Fig. 6. Normalized estimated DoA patterns (solid lines) for the source placed at three different angles in the azimuthal plane. The cross mark points to the actual position.

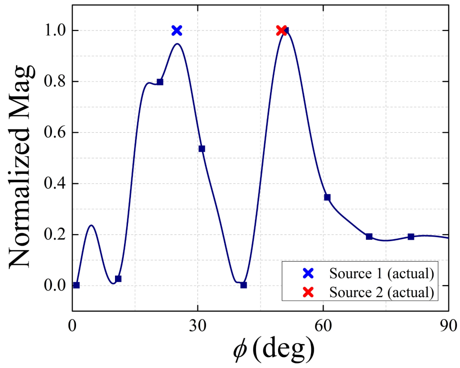

Fig. 7. Normalized estimated DoA pattern for the studied multi-source scenario.

results are shown in Fig. 7, where the DoAs are identified from the peaks in the calculated and normalized $\mathbf{f}$. The antenna correctly estimates the angle of the source at 25° and detecting the second source with an error of 1° at 51° for the actual 50° case.

V. CONCLUSION

In this paper, we proposed an SIW-integrated DMA design offering a wide beam coverage and can estimate the DoA for transmitting sources. When fed through both ports, it achieves an azimuthal coverage of 136°. The beams generated by biasing the p-i-n diodes with the patterns listed in Table I were used to detect the sources. The proposed DMA was validated through full-wave simulations in CST Studio Suite. Its planar configuration allows seamless integration with other RF front-end components. The combination of wide beam coverage and beam steering capability makes it well-suited for ISAC applications.

REFERENCES

[1] K. Wu, Z. Wang, S.-L. Chen, J. A. Zhang, and Y. J. Guo, "Isac: From human to environmental sensing," *IEEE Journal of Selected Topics in Electromagnetics, Antennas and Propagation*, pp. 1–15, 2025.

[2] Y. Cui, F. Liu, X. Jing, and J. Mu, "Integrating sensing and communications for ubiquitous iot: Applications, trends, and challenges," *IEEE Network*, vol. 35, no. 5, pp. 158–167, 2021.

[3] S. Waqar and M. Pätzold, "A simulation-based framework for the design of human activity recognition systems using radar sensors," *IEEE Internet of Things Journal*, vol. 11, no. 8, pp. 14 494–14 507, 2024.

[4] M. E. Gharbi, J. Abounasr, R. Fernández-García, and I. Gil, "A smart belt with embroidered antenna-based sensor for real-time respiratory monitoring," *IEEE Sensors Journal*, pp. 1–1, 2025.

[5] A. M. Molaei, P. del Hougne, V. Fusco, and O. Yurduseven, "Efficient joint estimation of doa, range and reflectivity in near-field by using mixed-order statistics and a symmetric mimo array," *IEEE Transactions on Vehicular Technology*, vol. 71, no. 3, pp. 2824–2842, 2022.

[6] A. M. Molaei, B. Zakeri, S. M. H. Andargoli, M. A. B. Abbasi, V. Fusco, and O. Yurduseven, "A comprehensive review of direction-of-arrival estimation and localization approaches in mixed-field sources scenario," *IEEE Access*, vol. 12, pp. 65 883–65 918, 2024.

[7] Z. Ebadi, A. M. Molaei, G. C. Alexandropoulos, M. A. B. Abbasi, S. Cotton, A. Tukmanov, and O. Yurduseven, "Near-field localization with antenna arrays in the presence of direction-dependent mutual coupling," *IEEE Transactions on Vehicular Technology*, vol. 74, no. 5, pp. 7033–7048, 2025.

[8] Z. Ebadi, A. M. Molaei, G. C. Alexandropoulos, M. A. Babar Abbasi, S. Cotton, A. Tukmanov, and O. Yurduseven, "Near-field localization with extremely large scale antenna arrays in the presence of mutual coupling," in *2025 19th European Conference on Antennas and Propagation (EuCAP)*, 2025, pp. 1–5.

[9] M. Ranjbar Nikkhah, J. Wu, H. Luyen, and N. Behdad, "A concurrently dual-polarized, simultaneous transmit and receive (star) antenna," *IEEE Transactions on Antennas and Propagation*, vol. 68, no. 8, pp. 5935–5944, 2020.

[10] L. Ma, C. Gu, and J. Mao, "A dual circularly polarized, simultaneous transmit and receive (star) common aperture antenna array for integrated sensing and communication," in *2022 IEEE Conference on Antenna Measurements and Applications (CAMA)*, 2022, pp. 1–3.

[11] L. Ma, J. Lai, Y. Yin, C. Xia, C. Gu, and J. Mao, "A wideband co-linearly polarized full-duplex antenna-in-package with high isolation for integrated sensing and communication," *IEEE Antennas and Wireless Propagation Letters*, vol. 22, no. 9, pp. 2185–2189, 2023.

[12] M. Zhao, L. Wang, S. Zhu, X. Chen, and O. Yurduseven, "Microwave integrated sensing and imaging using reconfigurable metacavity," *IEEE Transactions on Microwave Theory and Techniques*, vol. 73, no. 8, pp. 5592–5606, 2025.

[13] P. Jain, S. Ghosh, S. Cotton, and O. Yurduseven, "Single layer sub-6 ghz leaky dynamic metasurface antenna with wide beam coverage," *IEEE Antennas and Wireless Propagation Letters*, pp. 1–5, 2025.

[14] G. Álvarez Narciandi, M. García-Fernández, V. Skouroliakou, and O. Yurduseven, "Dynamic metasurface antenna-based mills-cross aperture for 3-d computational microwave imaging," *IEEE Antennas and Wireless Propagation Letters*, vol. 23, no. 11, pp. 3377–3381, 2024.

[15] M. Boyarsky, T. Sleasman, L. Pulido-Mancera, A. V. Diebold, M. F. Imani, and D. R. Smith, "Single-frequency 3d synthetic aperture imaging with dynamic metasurface antennas," *Appl. Opt.*, vol. 57, no. 15, pp. 4123–4134, May 2018. [Online]. Available: https://opg.optica.org/ao/abstract.cfm?URI=ao-57-15-4123

[16] M. Lin, X. Huang, B. Deng, J. Zhang, D. Guan, D. Yu, and Y. Qin, "A high-efficiency reconfigurable element for dynamic metasurface antenna," *IEEE Access*, vol. 8, pp. 87 446–87 455, 2020.

[17] "Ma4sps402," Macom.com, 2023. [Online]. Available: https://www.macom.com/products/product-detail/MA4SPS402

[18] D. Deslandes and K. Wu, "Accurate modeling, wave mechanisms, and design considerations of a substrate integrated waveguide," *IEEE Trans. Microwave Theory Techn.*, vol. 54, no. 6, pp. 2516–2526, Jun. 2006.

[19] F. Falcone, T. Lopetegi, M. A. G. Laso, J. D. Baena, J. Bonache, M. Beruete, R. Marqués, F. Martín, and M. Sorolla, "Babinet Principle applied to the design of metasurfaces and metamaterials," *Phys. Rev. Lett.*, vol. 93, no. 19, Nov. 2004.

[20] M. Johnson, P. Bowen, N. Kundtz, and A. Bily, “Discrete-dipole approximation model for control and optimization of a holographic metamaterial antenna,” *Appl. Opt.*, vol. 53, no. 25, p. 5791, Sep. 2014.

[21] D. R. Smith, O. Yurduseven, L. P. Mancera, P. Bowen, and N. B. Kundtz, “Analysis of a waveguide-fed metasurface antenna,” *Phys. Rev. Applied*, vol. 8, no. 5, Nov. 2017, publisher: American Physical Society (APS).

[22] A. Li, M. Zhao, M. A. B. Abbasi, and O. Yurduseven, “A measurement mode selection method for computational microwave imaging,” *IEEE Antennas and Wireless Propagation Letters*, vol. 23, no. 11, pp. 3382–3386, 2024.

[23] R. Kumar, G. Álvarez Narciandi, M. García-Fernández, V. Fusco, and O. Yurduseven, “Computational microwave imaging based on a single electric-field scan,” in *2022 19th European Radar Conference (EuRAD)*, 2022, pp. 1–4.

[24] Y. Saad and M. H. Schultz, “Gmres: A generalized minimal residual algorithm for solving nonsymmetric linear systems,” *SIAM Journal on Scientific and Statistical Computing*, vol. 7, no. 3, pp. 856–869, 1986. [Online]. Available: https://doi.org/10.1137/0907058